A Broadband Sensor for Permittivity Measurement of Solid, Crystal Grain, and Powder Dielectrics in Microwave Range

Mojtaba Joodaki, *Senior Member, IEEE*, Roshan Nepal, *Graduate Student Member, IEEE*, and Ali Shourvarzi

***Abstract*—This study presents a novel and accurate solution for measuring the real and imaginary parts of permittivity in a wide range of dielectrics. The proposed sensor, featuring a compact metal enclosure and a rectangular aperture, is a valuable tool for microwave characterization of different dielectrics. The study encompasses both theoretical and experimental approaches, combining finite element simulations to showcase the sensor's accuracy in diverse environments and with different material forms such as solid, crystal grain, and powder. A series of experiments were conducted using four sensors with varying enclosure dimensions, allowing for comprehensive measurements of complex permittivity within the frequency range of 3–15 GHz. The proposed sensor not only provides high accuracy but also offers a cost-effective and efficient solution for permittivity measurements. It requires only a small sample volume and eliminates the need for complex sample preparation procedures. This research demonstrates a promising alternative to conventional techniques used for permittivity measurement, opening up new methods for investigating dielectric properties in a variety of industrial and research settings.**

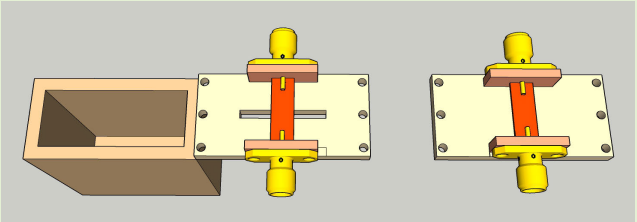

***Index Terms*— Broadband sensing, complex permittivity measurement, material characterization, microwave sensor, resonance, scattering parameters.**

I. Introduction

MICROWAVE sensing and characterization are rapidly advancing, yielding new insights and innovations [1], [2], [3], [4]. Several microwave and electromagnetic sensors have been developed to cater to diverse applications and requirements [5], [6], [7], [8], [9]. These advancements not only enhance our understanding of electromagnetic interactions but also pave the way for novel applications across various domains [10], [11], [12], [13], [14]. Accurate measurement of relative permittivity is important for understanding material behavior. Relative permittivity, denoted as ϵ_r, signifies a material's capacity to store and transmit electrical energy, influencing electronic device design and solutions for electromagnetic interference (EMI)/electromagnetic compatibility (EMC).

Dielectric materials are crucial in numerous applications across industry, science, and medicine. Precise measurement of high-frequency behavior, particularly relative permittivity, is important for effective EMI/EMC design. The complex permittivity $\epsilon_r(f) = \epsilon_r'(f) - i\epsilon_r''(f)$, where $\epsilon_r'(f)$ and $\epsilon_r''(f)$ represent the real and imaginary parts, respectively, which provides insights into dielectric materials' electrical properties [15], [16], [17], [18].

In this research, we quantify complex permittivity across materials using a method that combines a strip transmission line, a metal plate with an aperture, and a short-circuited rectangular waveguide as a metallic cavity. The results are validated by electromagnetic simulations and comparisons with results from other methods, which makes the approach applicable to solids, crystals, and powders. Numerous approaches have been developed to characterize materials by measuring

Manuscript received 12 January 2024; accepted 30 January 2024. Date of publication 16 February 2024; date of current version 2 April 2024. The associate editor coordinating the review of this article and approving it for publication was Dr. Wensong Wang. *(Corresponding author: Mojtaba Joodaki.)*

Mojtaba Joodaki is with the School of Computer Science and Engineering, Constructor University, Campus Ring 1, 28759 Bremen, Germany, on leave from the Department of Electrical Engineering, Ferdowsi University of Mashhad, Mashhad 9177948974, Iran (e-mail: mjoodaki@constructor.university).

Roshan Nepal was with the School of Computer Science and Engineering, Constructor University, Campus Ring 1, 28759 Bremen, Germany. He is now with the Department of Electrical and Computer Engineering (ECE), University of Waterloo, Waterloo, ON N2L 3G1, Canada (e-mail: roshan.nepal@uwaterloo.ca).

Ali Shourvarzi is with the Department of Electrical Engineering, Ferdowsi University of Mashhad, Mashhad 9177948974, Iran (e-mail: ali.shourvarzi@mail.um.ac.ir).

Digital Object Identifier 10.1109/JSEN.2024.3362698

their complex permittivity within the RF/microwave spectrum. Some of the most common techniques include cavity resonance, quality factors, transmission lines, split-ring resonators, and free-space techniques [19], [20], [21], [22], [23], [24], [25]. The selection of an appropriate method is contingent upon factors such as the operating frequency, the physical state of the sample, and its losses and volume.

The resonant method measures the Q-factor and resonant frequency of a material-filled resonant cavity to calculate its complex permittivity [19], [20], [26], [27], [28]. This method is particularly suitable for microwave frequencies and nondestructive measurements. On the other hand, the transmission/reflection line method involves measuring S-parameters of a waveguide setup including a layer of the material [29], [30], [31], [32], [33]. These parameters provide insights into the dielectric constant and magnetic permeability. Precision is maintained through proper calibration and careful setup design. In comparison, the free-space method focuses on the placement of the material between two antennas, enabling measurements across a broad frequency range, even under challenging conditions [34], [35], [36]. For liquids, the open-ended coaxial probe method is generally used, where reference liquids are used for calibration. The probe is immersed in the liquid, and the S-parameters are measured to determine the permittivity [37]. The open-ended waveguides are used in measurements of radiation properties and material properties [38], [39], [40]. They are used to measure the permittivity of materials, which is related to physical characteristics such as moisture content. Moreover, the split-ring resonator method provides accurate and noninvasive measurement but requires different prototypes for different applications, especially for materials of different forms [41], [42], [43]. Furthermore, the open resonator is a hybrid resonant technique based on the Fabry–Perot-type measurement [44], [45], [46]. It measures multiple resonances of the sample across a frequency range. The CPW or microstrip transmission line method offers a compact and integrable design for complex permittivity measurements, but its accuracy is limited by substrate and environmental factors, necessitating further development and validation for each application [47], [48].

These methods present diverse solutions for characterizing the dielectric properties of materials, each with distinct advantages and limitations. The choice of method depends on the specific characteristics of the material and the intended application. However, each method has its limitations associated with narrowband measurements, the complexity of setups, and constraints when working with particular dielectric materials (Table I).

Our sensor offers a distinct advantage among the existing measurement techniques. Although it derives its foundation from the resonant method, it overcomes several key challenges and limitations posed by conventional methods. It delivers precise broadband measurements of both the real and imaginary permittivity components, ensuring accuracy in measurements while minimizing setup complexity. Furthermore, its unique strength lies in its ability to characterize a broad spectrum of dielectrics, encompassing solids, powders, and crystal grains. In contrast, most of the existing methods are limited to specific materials or forms. Specially designed for materials with low to medium losses, the sensor operates effectively across a wide temperature range. The box-like design ensures simplicity and versatility across diverse applications while maintaining consistent performance. This design stands in contrast to the often intricate setups required by other methods, further highlighting the sensor's unique advantages. Table I provides a detailed comparison between various measurement methods and our novel sensor. It highlights the unique advantages of the sensor, including precise broadband measurements, versatility across different dielectric materials, operational effectiveness in a wide temperature range, and simplicity in setup.

Moreover, to determine the dielectric constant of materials, solving a set of complex nonlinear equations that relate the S-parameters of the sample to its dielectric properties is necessary. The existing methods often rely on assumptions or approximations, impacting result accuracy. For instance, the Nicholson–Ross–Weir (NRW) method assumes a flat response in the characteristic impedance near half-wavelength resonance frequencies, potentially leading to errors for low-loss or nondispersive materials [49], [50]. The National Institute of Standards and Technology (NIST) iterative method is another technique that uses an iterative approach to solve nonlinear equations, but it requires an initial guess of permittivity value and may fail to converge if the guess is not close to true values [51], [52]. In contrast to these common methods, we propose a novel numerical method related to the shielding effectiveness (SE) of the material sample [53], [54], [55], [56]. With this method, we first calculate the initial value of ϵ_r' accurately using the first resonant frequency of the sample and then use this value as the initial value to solve the nonlinear equations for the neighboring frequencies. In this way, wideband permittivity calculations are performed. This method does not make any assumptions or approximations that may affect the accuracy of the results, and it can be used for a wide range of materials with different dielectric properties.

Section II outlines the methodology, including measurement setup and sample preparation. Section III validates the proposed method through simulations and comparisons, demonstrating accuracy. Section IV presents the experimental results confirming its efficacy across materials. Section V provides a comparative analysis of sensors, considering dimensions and materials. It also evaluates performance in terms of accuracy, reliability, and temperature sensitivity. Section VI summarizes the findings and discusses applications.

II. Methodology

The sensor is based on a small enclosure with an aperture, which serves as the basic element. The sensor is designed to measure the dielectric constant of solid, crystal, and powdered materials. The sensor works by placing a strip line (SL) over the ground plane with an aperture as shown in Fig. 1. An SL acts as a type of transmission line used to transfer microwave signals between components, which are then analyzed to determine the impedance between the ports.

A. Aperture Impedance

In Fig. 1(a), a metallic enclosure with an aperture is shown as part of the measurement setup with a two-port network.

TABLE I
OVERVIEW OF DIFFERENT METHODS USED IN DIELECTRIC PERMITTIVITY MEASUREMENT

Method	Applications	Advantages	Disadvantages
Cavity Resonant [26]–[28], [30]	Materials with low-to-high loss	Accurate real permittivity readings; non-contact approach	Narrow bandwidth; can be destructive for solids; limited by the size and physical state of the sample
Free-space [30], [34]–[36]	Primarily block solids with variable losses	Non-contact method; ultra-wideband; non-destructive	Demands specific Material Under Test (MUT) attributes; may have less accuracy
Transmission and Reflection line [30]–[33]	Suitable for materials with medium to high losses	Wide bandwidth; high accuracy; non-destructive; simple design	Necessitates specific de-embedding and calibration
Open-ended Coaxial Probe [29], [37], [57]	Non-destructive testing; ideal for materials with low losses	Accurate readings; do not need sample alignment; allows for temperature moderation	Solely reflection-based; sensitivity to air gaps; need to solve complex mathematical model
Open-ended Waveguide [38]–[40]	Non-destructive testing; ideal for materials with low losses	Similar to open-ended coaxial probe but better optimized for measurements on lower permittivity materials	Sensitive to air gaps; multiple repeated measurements needed for reliable result; complexity in obtaining good contact with center of conductor
Split-ring resonator [41]–[43]	Broadband measurement; non-contact sensing, mixture characterization; suitable for materials with medium to high losses	Highly accurate; non-invasive; continuous glucose level monitoring; sensor's quality factor enhancement	Separate prototypes needed for other material forms; cross-sensitive to measurement errors and environmental conditions
Open resonator [44]–[46]	Broadband measurement; non-destructive; testing suitable for low-loss laminar dielectric materials	High accuracy; good quality factor measurement; multi-frequency measurements	Large sample size needed; system calibration required
Coplanar waveguide (CPW) or microstrip [47], [48]	Broadband measurement; non-destructive testing; high-frequency application	Applicable for solids and liquids; compact design; ease of fabrication; planar configuration	Sensitivity to substrate properties and temperature; additional development and validation required for each application
Our method	Broadband measurement; non-destructive testing	Applicable to solids, grains, and powder; wide bandwidth; simple setup; accurate readings; usable at various temperatures; no need for sample alignment	Not ideal for high-loss materials and liquids (see Section V-E)

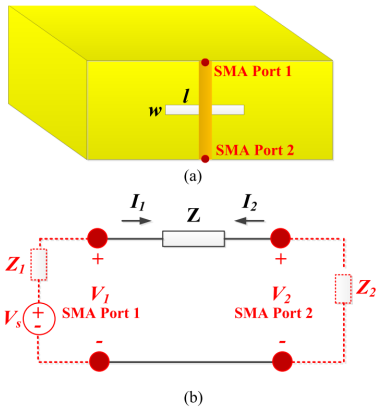

Fig. 1. (a) Design of the sensor enclosure with an aperture, and an SL with the enclosure body serving as its ground plane. (b) Two-port equivalent network for the configuration shown in (a) [56].

Ports are connected to the enclosure such that one end of each port (ground) is terminated at the enclosure's plate, while the other end (signal) connects to a metallic strip. The aperture is treated as a transmission line with a defect in the ground such that the impedance of the aperture can be measured. To accurately measure the impedance change caused by filling the cavity, we performed three impedance measurements under different conditions. First, we measured the impedance with the lid closed and no aperture present. Next, we measured the impedance with the aperture present and the cavity empty. Finally, we measured the impedance with the aperture present and the cavity filled. Since the aperture is not filled with the measurand in the second reference measurement, thus to have an accurate de-embedding process, the gap in the aperture should be empty when the cavity is filled with the measurand as well.

The analysis uses the circuit depicted in Fig. 1(b), encompassing load impedance (Z_l), source impedance (Z_s), and interport impedance (Z). For nonzero impedance ($Z \neq 0$) between these ports, the relationship between the S-parameters and Z is established as follows [53], [54], [55], [56], [58]:

$$Z = \frac{2Z_o S_{11}}{1 - S_{11}} \quad \text{or} \quad Z = \frac{2Z_o\,(1 - S_{21})}{S_{21}} \tag{1}$$

where Z_o is the characteristic impedance of the transmission line.

Fig. 2 displays the simulated structure, consisting of an SL on top, two ports connected to the enclosure as their ground, and an enclosure with an aperture. This system corresponds to a two-port network configuration, as shown in Fig. 3. An aperture-free setup with properly designed SL specifications would yield a zero impedance ($Z = 0$), forming a 50-Ω line. However, any aperture or ground plane defect increases resistance and leads to a nonzero impedance.

Equation (1) calculates the nonzero impedance (Z) using both the magnitude and the phase of the measured S-parameters. The aperture impedance (Z_{ap}) is analogous to an impedance across coplanar SL with both the ends effectively shortened due to its location on the enclosure's face.

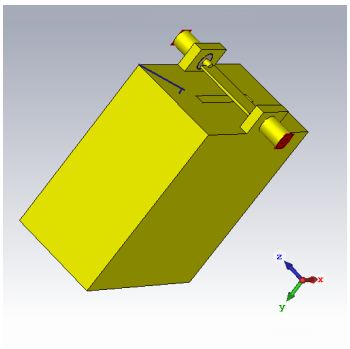

Fig. 2. Simulated 3-D diagram of the sensor designed in CST Studio Suite with dimensions of 40 × 40 × 20 mm. Aperture of 20 × 2 mm ($l \times w$) and SL of 14 × 5 mm, 1.9 mm above the lid surface. The trace's direction is perpendicular to the larger side of the aperture [54].

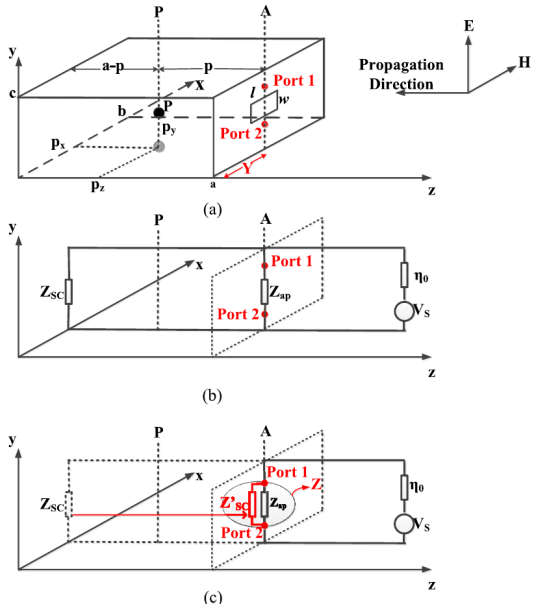

Fig. 3. (a) Sensor apparatus (enclosure with aperture excited by SL). (b) Circuit model of the sensor. (c) Circuit model with Z_{sc} transferred to the aperture (point A) [24], [56].

The characteristic impedance (Z_g) and propagation constant (k_g) for the TE_{10} mode within the enclosure's waveguide are

$$k_g = k_0\sqrt{1-\left(\frac{\lambda}{2b}\right)^2} \tag{2}$$

$$Z_g = \eta_0\sqrt{1-\left(\frac{\lambda}{2b}\right)^2}. \tag{3}$$

Here, $k_0 = (2\pi/\lambda)$ is the wavenumber, $\eta_0 = 377\Omega$ is the free-space impedance, b is the waveguide width, and λ is the free-space wavelength.

The enclosure's frontal surface efficiently reflects a short-circuit impedance at the termination point, leading to

$$Z'_{\text{sc}} = jZ_g \tan\left(k_g a\right). \tag{4}$$

The parallel combination of aperture impedance (Z_{ap}) and transferred enclosure short-circuit (Z'_{sc}) yields Z

$$Z = Z_{\text{ap}} \parallel Z'_{\text{sc}}. \tag{5}$$

Thus, aperture impedance (Z_{ap}) can be calculated using the formula

$$Z_{\text{ap}} = \frac{ZZ'_{\text{sc}}}{Z'_{\text{sc}} - Z}. \tag{6}$$

B. Real Part of Dielectric Constant, ϵ'_r Formulation

In Section II-A, the metallic enclosure was empty, i.e., filled with air or vacuum. When the enclosure is completely filled with a dielectric material up to the bottom of the enclosure, the relative permittivity of the material should be taken into account to calculate the propagation constant and characteristic impedance of the waveguide. The transferred Z_{sc} at the terminal face of the enclosure is represented as Z''_{sc}, and its expression is defined as follows:

$$Z''_{\text{sc}} = jZ'_g \tan\left(k'_g a\right) \tag{7}$$

$$k'_g = k_0\sqrt{1-\left(\frac{\lambda_m}{2b}\right)^2} \tag{8}$$

$$Z'_g = \eta_0\sqrt{1-\left(\frac{\lambda_m}{2b}\right)^2}. \tag{9}$$

In these equations, Z''_{sc} is the short-circuit impedance when the box is filled, k'_g is the modified propagation constant, and Z'_g is the modified characteristic impedance. The value of k'_g is determined by (8).

The wavelength of the medium, λ_m, is represented by

$$\lambda_m = \frac{\lambda}{\sqrt{\epsilon'_r}} \tag{10}$$

where ϵ'_r is the real part of the relative permittivity.

When the S-parameter is measured again with the enclosure filled with a dielectric material, a different impedance (Z) will be observed between the two ports in Fig. 1. However, since the aperture impedance (Z_{ap}) remains the same for both the cases, the short-circuit impedance (Z''_{sc}) can be estimated.

This estimation allows for the calculation of ϵ'_r of the material within the enclosure using (7)–(10). To simplify and shorten the numerical procedure, the resonance frequencies and their shifts can be considered. The shifts of the resonance frequencies have a dependency of $1/(\epsilon'_r)^{1/2}$ referring to (10). These resonant frequency values can be used as starting points to solve the nonlinear equations (4) and (7), providing a frequency-varying response for the wavelength of the medium. Thus, the ϵ'_r at the resonance frequencies can be calculated, and regression between these points can provide its behavior against the frequency. It should be noted that although the technique provides a broad frequency-dependent response, the results are less reliable for frequencies below the first resonance frequency of the enclosure.

C. Imaginary Part of Dielectric Constant, ϵ''_r Formulation

In a prior investigation [54], the focus was on deriving the SE and formulating the voltage at a monitor point (v_p). The leakage voltage, v_p, is the voltage that appears at the monitoring point due to the presence of an aperture in the

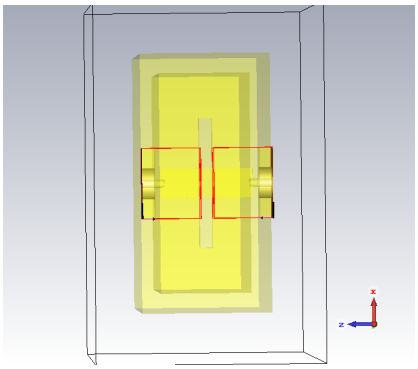

Fig. 4. Top view of the enclosure, where the de-embedding technique has been used from the ports up to the periphery of the aperture.

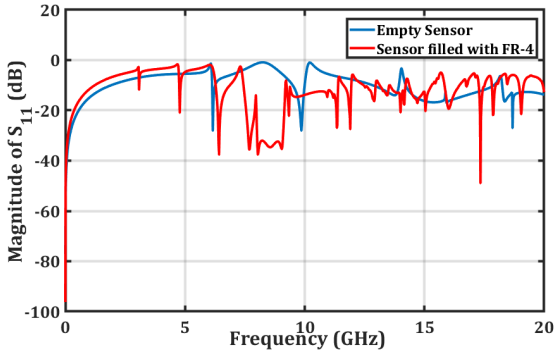

Fig. 5. Simulated S_{11} results of empty medium enclosure and the enclosure filled with FR-4. Both the results are de-embedded up to the periphery of the aperture.

shielded enclosure. It arises from the radiated energy emitted by the aperture.

When a new dielectric material is introduced into the enclosure, its relative permittivity changes, influencing wave propagation within the enclosure. Consequently, the short-circuit impedance shifts, leading to a modification in the leakage voltage. This altered leakage voltage is denoted as v_p'. This relative loss can be succinctly expressed as the ratio (v_p/v_p'), and its formulation is provided as follows [59]:

$$\frac{v_p}{v_p'} = e^{-\frac{2\pi}{\lambda}\epsilon_r'' p} \tag{11}$$

where λ denotes the electromagnetic wave's wavelength, p is the distance between the aperture and the monitoring point, and ϵ_r'' signifies the imaginary part of the relative permittivity, which can be obtained as

$$\epsilon_r'' = -\frac{\lambda \ln\left(\frac{v_p}{v_p'}\right)}{2\pi p}. \tag{12}$$

D. De-Embedding

To accurately determine the impedance Z using (1), it is important to account for the parasitic effects introduced by the SMA connectors and SL. To remove these effects, short, open, load, and through (SOLT) calibration up to the SMA connectors and de-embedding up to the aperture edges are required.

De-embedding is a simple method that can be used to remove these effects in simulation. For both the simulated and experimental results, we performed a de-embedding procedure as described in [56]. For the simulated results, we can calibrate the results to the aperture edges using the postprocessing tab, as shown in Fig. 4. For the experimental results, the S-parameters for the sensor with aperture are compared with those of the sensor without aperture. This process can help eliminate undesired reflections and distortions in the measured data, resulting in more accurate and reliable simulation results.

III. Simulation Results

The simulations were conducted to investigate the electromagnetic characteristics of the enclosure and its components, including the dielectric material. The results of these simulations provide valuable insights into the performance of the proposed design and its potential for practical applications. The simulation results are presented in Section III-B.

A. 3-D Design

The 3-D design of the sensor involved creating a 40 × 40 × 20 mm box with a hollow interior made of copper with a thickness of 3 mm, similar to the simulated design as shown in Fig. 2. The lid of the sensor was also made of copper with a thickness of 3 mm. An aperture of length of 20 mm and width of 2 mm was placed in the center of the lid, while a reference model without the aperture was also created to provide a comparison for the de-embedding process. The 3-D model was fabricated for use in the experiment, and the results were compared with those obtained through simulation.

B. 3-D Full-Wave Simulation

To further evaluate the electromagnetic properties of the sensor and the effect of the dielectric material on it, a simulation was performed using the Frequency Domain Solver of CST Studio Suite. The model was designed for simulations in the frequency range of 0–20 GHz. An SL was placed on top of the lid to investigate its response to electromagnetic fields. The S-parameters were evaluated for the empty box and the box filled with FR-4 as the dielectric material for further calculations. The results were de-embedded up to the aperture edges to accurately measure the electromagnetic behavior. The simulation results are shown in Fig. 5.

C. Validation Procedures

For a better theoretical validation of our measurement method, the first 3-D full-wave simulations are performed using our sensor filled with a lossy dielectric material with a Gaussian permittivity and linear loss tangent profile versus frequency. Fig. 6 illustrates the comparison of the extracted ϵ_r' and $\tan\delta$ values from simulations to the corresponding simulation-generated curves. This analysis demonstrates a clear alignment between the two datasets. Our study's measurement approach proves its precision and reliability in determining the relative permittivity of various dielectric materials.

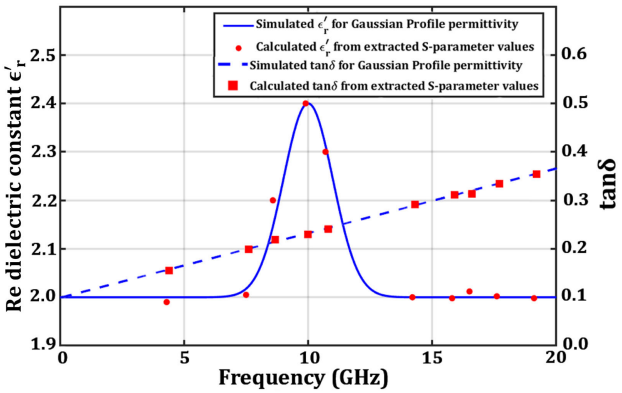

Fig. 6. Comparison of the simulated results of a material featuring Gaussian profile permittivity with the real part of permittivity (left *y*-axis) and loss tangent (right *y*-axis) values obtained through our method on the extracted S-parameters.

IV. Experimental Results

The experimental section of this work involved a thorough investigation of the performance of a range of sensors made from copper and aluminum in measuring the complex permittivity of various materials in different forms. To carry out this investigation, we carefully selected sensors with different dimensions and characteristics to ensure that we covered a wide range of measurement scenarios.

During the experiments, we compared the sensors for their accuracy, reliability, range, and feasibility, taking into account various factors such as the size and shape of the materials, and the intended application of the sensors. We also evaluated the sensors for their sensitivity, stability, and repeatability, which are important parameters that determine the quality of the measurements.

A. Measurement Setup

The following are the dimensions of the sensors that are used to test the materials.

1) $80 \times 40 \times 20$ mm (big copper sensor, Fig. 7).
2) $40 \times 40 \times 20$ mm (medium copper sensor).
3) $20 \times 40 \times 20$ mm (small copper sensor).
4) $20 \times 40 \times 20$ mm (small aluminum sensor).

The sensor is connected to the Rohde & Schwarz VNA, and the wires are clamped on the side to minimize shaking of the wires. The S-parameters are calculated for the lid without an aperture, the empty box with a lid with an aperture, and the box filled with materials. The results for the lid without an aperture are used to de-embed the results across the aperture. The results are then evaluated to calculate the complex permittivity.

The materials that were tested in this experiment included solids, powders, and crystal grains, which were selected based on their diverse dielectric properties. The materials were tightly filled into the enclosure and discarded after the measurements. The enclosure was thoroughly cleaned to guarantee the absence of any residue for subsequent tests with different materials. To ensure measurement accuracy through multiple trials, unused materials were used for crystals and powders, while the same block was used for solid samples. To calculate the dielectric constant of the materials, we used the principle

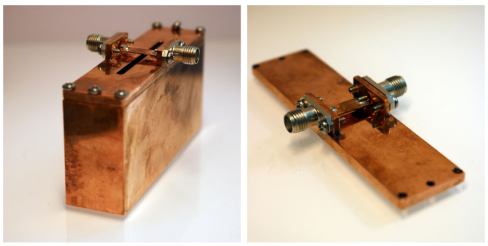

Fig. 7. (a) Fabricated big copper sensor with a large aperture (40×2 mm) and an SL (16×5 mm, thickness 0.5 mm) located 2 mm from the lid surface. (b) Lid without an aperture used for de-embedding S-parameters up to the aperture edges.

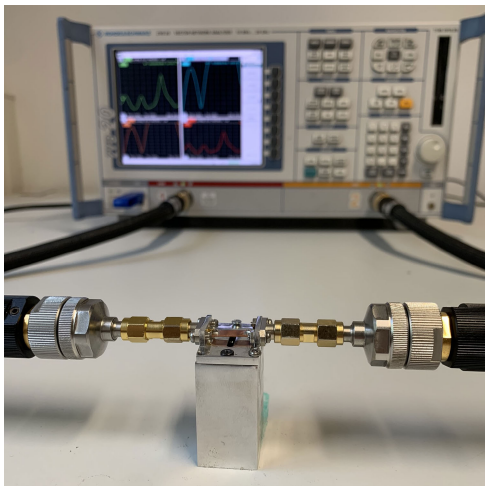

Fig. 8. Measurement setup, with a small aluminum sensor connected to the R&S VNA. The position of the sensor is fixed with a marker so that all the measurements are carried out at the same position.

of operation described in Section II. The materials were placed inside the sensors, and the measurements were carried out using the measurement setup shown in Fig. 8.

B. Common Salt (NaCl)

Two types of salt were tested: an iodized (Jodiertes Speisesalz) and salt without iodine (Alpen Salz). The salt was filled into the box and gently shaken to allow it to evenly settle inside the enclosure, and more salt was added until the box was fully covered with salt, as shown in Fig. 9. The complex permittivity of salt was calculated and compared for copper and aluminum boxes. Fig. 10 displays ϵ_r' and tanδ for salts with and without iodine and compares the values for copper and aluminum sensors.

Although there is a small difference in the values of the dielectric constant between the two materials, we were not sure whether this was due to the small iodine content in the salt (around 0.2%). Other uncontrolled factors such as salts' purity and environment humidity might cause such minor effects. It is worth noting that with a higher iodine content, the values would likely differ more substantially.

However, a distinct deviation was noted when the aluminum sensor was filled with iodine-laced salt, prominently within the 8–11-GHz frequency range. This behavior could be linked to aluminum's inherent oxidation in air, leading to the formation

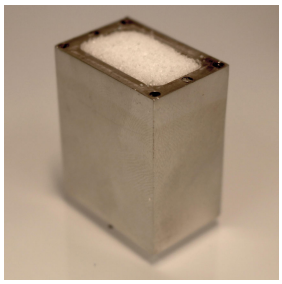

Fig. 9. Small aluminum box filled with salt.

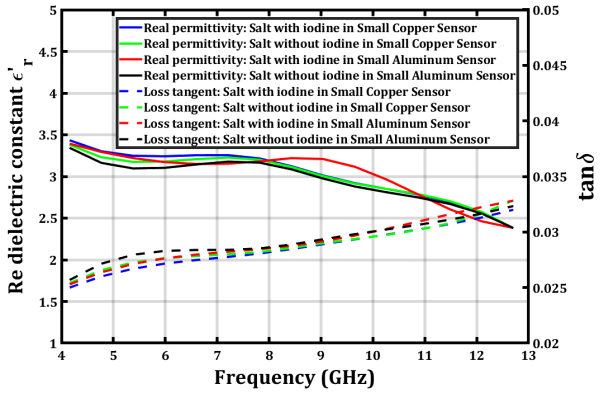

Fig. 10. Measured real (left *y*-axis) part of permittivity and loss tangent (right *y*-axis) against frequency for salt with and without iodine. In this experiment, small size boxes made of aluminum and copper are used.

of an aluminum oxide layer on the surface of the sensor [60]. Within the specified frequency range, a resonant interaction might occur between this oxide layer and the iodine in the salt, amplifying their dielectric interactions. While these initial findings hint at the aluminum sensor's potential for iodine detection in salt, further research, particularly focusing on resonance effects and dielectric interplay, is crucial for validation. Therefore, copper sensors are preferred for common complex dielectric constant measurements.

In a previous work, Liu et al. [61] determined the permittivity of NaCl with varying moisture levels, finding that the real part ranges between 2 and 5. Our results are comparable to these findings. Moreover, tanδ of the salts is slightly higher for aluminum sensor than that for the copper sensor, indicating that the aluminum sensor absorbs more energy from the wave than the copper sensor. This can be attributed to the fact that aluminum has a higher resistivity than copper, which leads to more energy dissipation.

C. Silica (SiO_2)

SiO_2 powders are widely used in high-frequency technology. Their dielectric properties and thermal stability make them essential in the production of electronic components such as capacitors, resonators, and integrated circuits. Their insulating properties also prevent unwanted electrical conduction, ensuring reliable performance in high-frequency devices across industries such as telecommunications and electronics.

Hence, studying silica's permittivity, particularly at high frequencies, is important. Hotta et al. [62] examined SiO_2 with varying relative densities across 3–13.5 GHz using silica

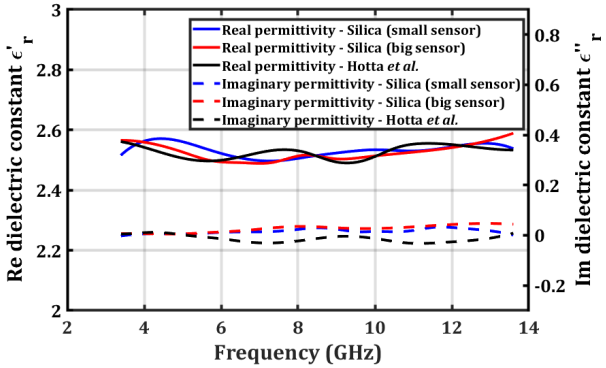

Fig. 11. Comparison of the measured real (left *y*-axis) and imaginary (right *y*-axis) part of permittivity against frequency for silica powder with the results from Hotta et al. [62]. In this experiment, small and big-sized copper sensors are used.

powder (average particle size of 36 μm) and relative densities of 46%–70%.

For our experiment, we used silica powder (particle size 40 μm, relative density 60%) as a dielectric in the medium and large boxes and measured the real and imaginary permittivity from 3 to 14 GHz, as depicted in Fig. 11. The filling process involved strongly shaking the powder to eliminate any air gaps, with successive rounds of refilling and shaking to densely occupy any remaining space within the enclosure. This approach was consistently applied to all the tested powders and crystals. Dielectric constants were compared with the results from Hotta et al. [62] for SiO_2 powder with 59.6% relative density.

We observe good agreement in ϵ_r' with Hotta et al.'s results, especially beyond 6 GHz. However, for ϵ_r'', our findings appear to be more dependable. A peculiar observation in the result from Hotta et al. [62] is the presence of a gain, indicated by a negative loss value, at higher frequencies. Such a phenomenon is not typically expected in these measurements and could point to potential anomalies or inconsistencies in their methodology or instrumentation. Our results, in contrast, do not exhibit this anomaly, increasing the reliability of our method.

D. Polyethylene Terephthalate

Polyethylene terephthalate (PET) is a versatile plastic used in various applications, including food packaging, textiles, and electronics. In electronics, PET is favored as a substrate for flexible printed circuits (FPCs) due to its lightweight, durability, and resistance to heat and moisture. We used a PET block from Röchling Group and it was cut to match the medium enclosure size, serving as a dielectric (Fig. 12).

We measured the complex permittivity of PET from 3 to 14 GHz, as depicted in Fig. 13. In a related study by Geryak et al. [63], the complex permittivity of PET sheets was investigated, covering a range of thicknesses from 1 to 10 mils and frequencies spanning 5–20 GHz. We compared our room temperature measurements, obtained from a 14-mm-thick PET with the results from Geryak et al. [63] for the thickness of 10 mils in Fig. 13. Our values align within their range of values, reinforcing the accuracy of our

Fig. 12. PET block placed in the enclosure of medium-sized sensor made of copper.

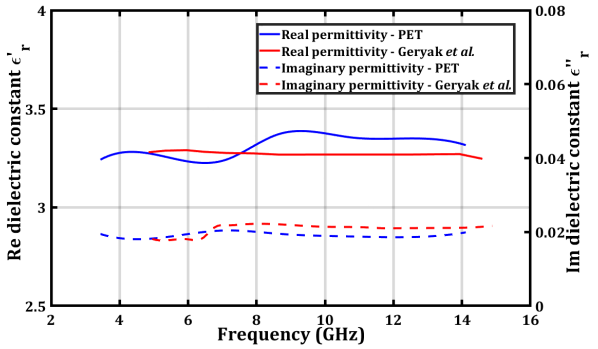

Fig. 13. Comparative analysis of real (left *y*-axis) and imaginary (right *y*-axis) permittivity components across frequency for PET, with reference to Geryak et al.'s [63] findings for a 10-mil-thick PET block. The measurements were conducted using a 14-mm PET block within the medium copper sensor.

measurements. However, it is imperative to acknowledge that direct comparisons may be limited due to the different thicknesses and purity levels inherent to PET samples.

E. Polymethyl Methacrylate or Plexiglass

Plexiglass is useful in thin-film form for high-frequency applications where its impact due to the high loss is reduced by thinner material. A Plexiglass block from RS Components International was cut to match the medium enclosure size and used as a dielectric. We measured the complex permittivity of polymethyl methacrylate (PMMA) from 4 to 14 GHz and compared them with the results from other method, as shown in Fig. 14.

We observed that ϵ'_r is slightly smaller compared with the results from the Nicolson–Ross technique [65]; however, our results have a better agreement with those of Deshpande et al. [64].

F. Magnesium Sulfate Heptahydrate ($MgSO_4 \cdot 7H_2O$)

Magnesium sulfate crystals (epsom salt), with formula $MgSO_4$, are used in medical and industrial settings. They are used as laxatives, for muscle cramp treatment, in agriculture, textiles, and paper production.

Our experiments used $MgSO_4 \cdot 7H_2O$ crystals (molar mass 246.48 g/mol) of high purity and size. The tests involved the small and large copper sensors, plus the small aluminum

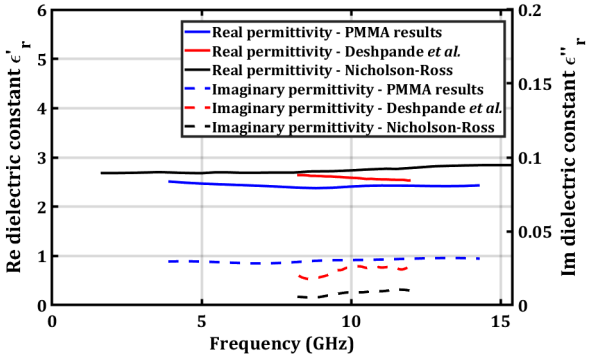

Fig. 14. Comparison of the measured real (left *y*-axis) and imaginary (left *y*-axis) parts of permittivity against frequency for PMMA filled in the medium copper sensor with the results of [64] and [65].

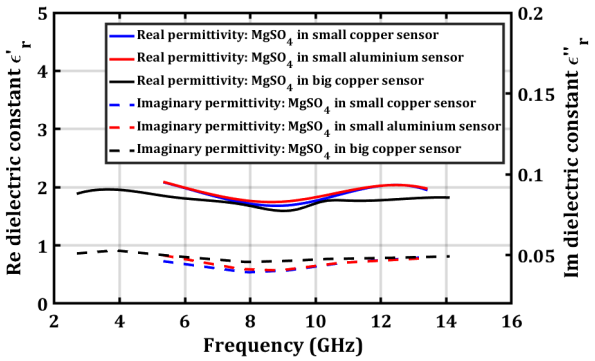

Fig. 15. Comparative analysis of real (left *y*-axis) and imaginary (right *y*-axis) parts of permittivity against frequency $MgSO_4 \cdot 7H_2O$ in various sensors. This experiment used both small-sized sensors, made from copper and aluminum, and large copper sensors.

sensor. Complex permittivity of $MgSO_4 \cdot 7H_2O$ was measured from 3 to 14 GHz, as shown in Fig. 15.

The comparative analysis of sensors provides consistent performance in terms of real permittivity measurements across the sensors. However, discrepancies become apparent when evaluating the imaginary components of permittivity. One plausible explanation for this deviation lies in the modal characteristics of the sensors. While our method predominantly considers the dominant mode, TE_{10}, it is necessary to recognize that in practical applications, the presence of higher order modes is unavoidable. These higher order modes exhibit loss characteristics. For sensors with larger dimensions, the propagation of a greater number of other modes is present when compared with the smaller ones. Consequently, the loss magnitude for larger sensors is slightly higher than that of smaller sensors at specific frequency bands.

G. Sugar

The study investigated fine sugar powder's permittivity using small and big copper sensors. "Feiner Zucker" from Nordzucker AG was used. We measured the complex permittivity of sugar from 3 to 16 GHz, as shown in Fig. 16.

The real part of the permittivity exhibits close alignment between the two sensors at higher frequencies; however, disparities can be observed for frequencies below 8 GHz. This difference arises primarily from the distinct resonance

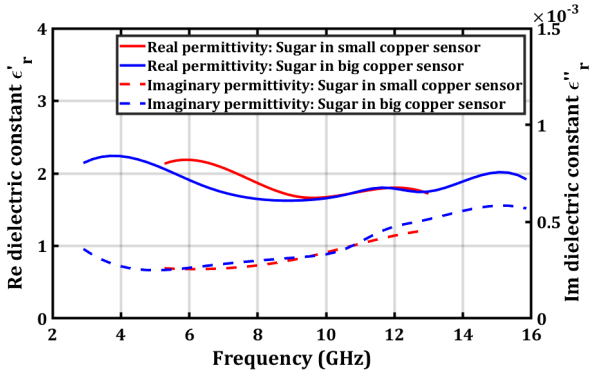

Fig. 16. Comparative analysis of real (left *y*-axis) and imaginary (right *y*-axis) parts of permittivity against frequency for sugar filled in the small and big copper sensors.

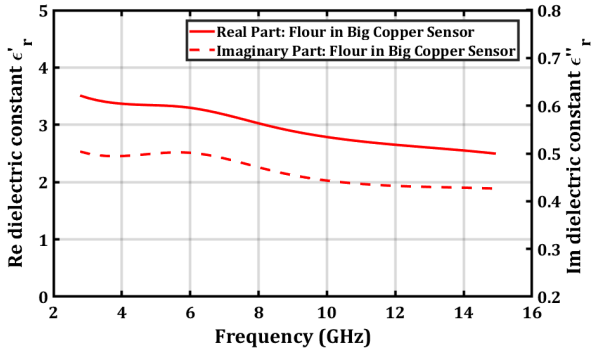

Fig. 17. Measured real (left *y*-axis) and imaginary (right *y*-axis) parts of permittivity against frequency for flour using the big copper sensor.

characteristics of the two sensors. Notably, the large copper sensor has its first resonance frequency at 4 GHz, while the small copper sensor has its first resonance at 8 GHz, thus contributing to the differentiation in the real part. Furthermore, the big sensor demonstrates a marginally higher imaginary component, attributed to the other propagation modes previously discussed in the context of $MgSO_4 \cdot 7H_2O$ results.

H. Flour

The flour's permittivity was investigated using the large copper box. The dielectric constant was studied from 3 to 15 GHz. The results in Fig. 17 show the frequency-dependent complex permittivity. The real part rises and the imaginary part decreases with increasing frequency. Flour's tanδ around 0.2 indicates moderate lossiness at these frequencies.

V. Sensor Properties and Performance Analysis

A. Comparison Based on Sensor's Dimension

This study investigated complex permittivity in solid, powder, and crystal forms using sensors with different dimensions and materials. The width of the enclosure has been set to 20 mm aligning with the length of the SL on top of the lid. In addition, the height of the sensor's enclosure was arbitrarily fixed at 40 mm, while variations in dimensions were introduced by altering the lengths to evaluate differences in the results.

One key observation was that complex permittivity values exhibited similarity above 6 GHz for the medium-sized sensor and 8 GHz for the small sensor. However, those sensors were less reliable at lower frequencies, primarily because of the absence of resonance below the above-mentioned frequencies, as shown in Figs. 10 and 15. It was noted that larger sensors demonstrated higher reliability at lower frequencies (Fig. 15). This advantage stemmed from their first resonance occurring at 4 GHz, a frequency range that was unattainable for smaller sensors. This implies that larger sensors may be more adept at providing more reliable measurements in scenarios where lower frequencies are of particular interest. Moreover, we have the flexibility to adjust the depth of the sensor's enclosure based on the frequency of interest, considering that the complex permittivity is more reliable at frequencies above the cutoff frequency of the enclosure. Hence, both the length and depth of the enclosure can be changed to align with the minimum required frequency of interest.

However, as observed in Figs. 15 and 16, bigger sensors exhibit higher loss due to the presence of higher modes compared with the smaller sensors. It should also be noted that larger sensors typically require more material, potentially making them less economical or convenient to handle in certain situations. Therefore, the choice of sensor size should be considered in the context of the specific application's frequency requirements, material availability, and ease of handling.

B. Comparison Based on Sensor's Material

The results were compared between the small copper and aluminum sensors to determine the difference in complex permittivity of dielectric based on the material used. Notably, aluminum sensors consistently showcased slightly higher loss levels (Fig. 10). This increased loss can be attributed to the higher resistivity of aluminum, compared with copper, which might have led to some energy dissipation at those particular frequencies in Fig. 10.

Moreover, we also examined the S-parameters for both empty and filled aluminum and copper sensors of identical dimensions, as illustrated in Figs. 18 and 19. Notably, despite measuring the same dielectric on sensors of the same sizes, we detected variations in frequency shifts. This variation can be attributed to a combination of factors. One of the predominant reasons might be the inherent measurement accuracy of the measurement facility including the VNA. Specifically, the loss inherent to each material may fall within the precision tolerance of the instrument used, making it challenging to distinguish between the two. Moreover, aluminium's inherent tendency to oxidize rapidly in ambient conditions results in the formation of a thin aluminum oxide layer. This oxide layer, particularly resonant at specific frequencies, can introduce added losses. Microstructural differences, grain boundaries, and impurities inherent to aluminum can further amplify dielectric losses at these resonant points. The difference is more visible when the sensors are filled with a dielectric material (Fig. 19), reinforcing the factors related to oxidation and dielectric interaction. Nevertheless, aluminum presents several advantages as well. Foremost, it has a lower density

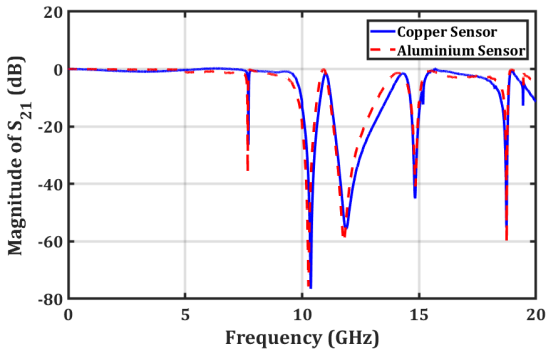

Fig. 18. Comparison of the de-embedded S_{21} for small-sized empty copper and aluminum sensors.

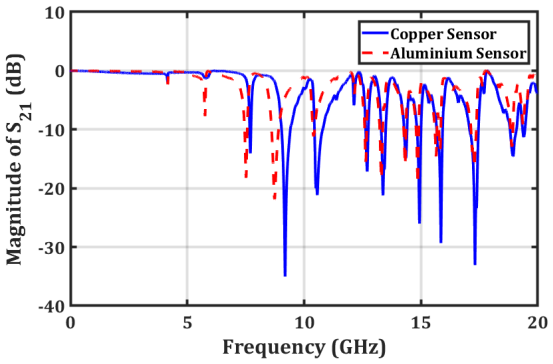

Fig. 19. Comparison of the measured de-embedded S_{21} for small-sized copper and aluminum sensors for salt with iodine.

TABLE II
COMPARISON OF SUITABILITY OF SENSORS FOR DIELECTRIC PERMITTIVITY MEASUREMENT

Requirement	Suitable Sensor
Compact size	Small Aluminium or Copper Sensor
Low Frequency	Big Copper Sensor
High Frequency	Small Aluminium or Copper Sensor
Broader frequency range	Big Copper Sensor

than copper, making it significantly lighter. Economically, aluminum is often more cost-effective than copper. In addition, the fabrication process for aluminum is relatively straightforward, enabling swift production and scalability.

Given the insights from our study on resonance frequencies and the effects of material-based losses over different frequency ranges, it becomes essential for researchers and engineers to carefully choose sensor materials for distinct applications, considering the balance between various performance characteristics. To further assist in this decision-making, we have provided a detailed comparison in Table II, highlighting the distinctions between various performance characteristics of each sensor.

C. Accuracy and Reliability

We averaged 32 measurements in the VNA to mitigate noise and enhance accuracy. This averaging strategy substantially reduces the potential for errors and noise, ensuring that our results are not only reliable but also highly accurate. We also

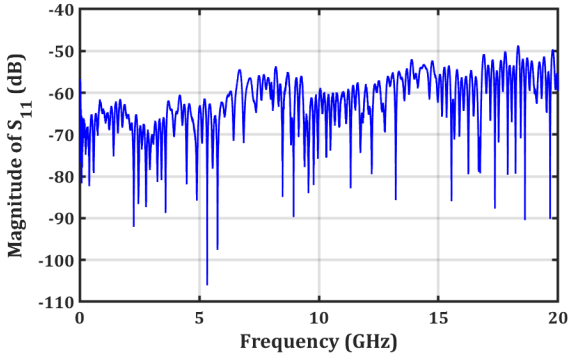

Fig. 20. S_{11} versus frequency for the calibrated load on port 1. The values are de-embedded up to the aperture edges.

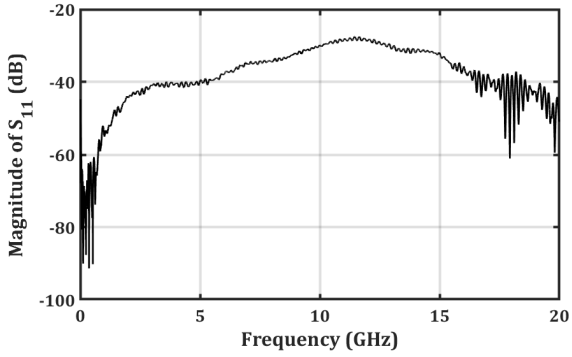

Fig. 21. S_{11} versus frequency for calibrated through after de-embedding. The values are de-embedded up to the aperture edges.

performed short, load, open, and through (SLOT) calibrations to correct systematic measurement errors.

After calibration, S_{11} measurements for the 50-Ω match showed values below −50 dB, as shown in Fig. 20, indicating successful impedance matching. The through measurement also showed low values (below −30 dB), as shown in Fig. 21, indicating minimal transmission loss. These results confirm accurate calibration and negligible transmission losses in measurements. In addition, the enclosure's lid is tightly fastened with six screws (Fig. 7), minimizing the influence of potential air gaps between the enclosure edge and the lid during measurements. Moreover, each of the experimental results is compared with the results from other researchers in Section IV, ensuring accuracy and reliability.

D. Variation in Permittivity With Temperature

We conducted experiments to analyze the variation in permittivity with temperature using $MgSO_4{\cdot}7H_2O$ material and the small aluminum sensor. The S-parameters for both empty and filled sensors were extracted at three different temperatures: 18.5 °C, 30 °C, and 50 °C.

When analyzing the S-parameters of the empty sensor across varying temperatures, it is apparent that while minute differences might not be immediately visible, they are notably evident when one closely examines or zooms in on the graph, as shown in Fig. 22. Moreover, as the temperature increases, a slight deviation in ϵ_r' of $MgSO_4{\cdot}7H_2O$ is observed, as shown in Fig. 23. The most distinct observation is the behavior of the loss tangent in Fig. 23. It is observed that the loss tangent

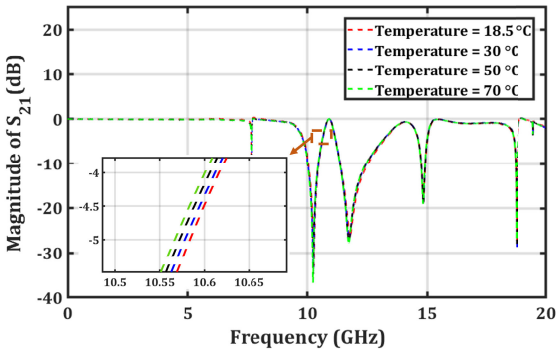

Fig. 22. S_{21} at different temperatures for the empty small aluminum sensor. along with a zoomed-in figure to show the small differences in the values with temperature.

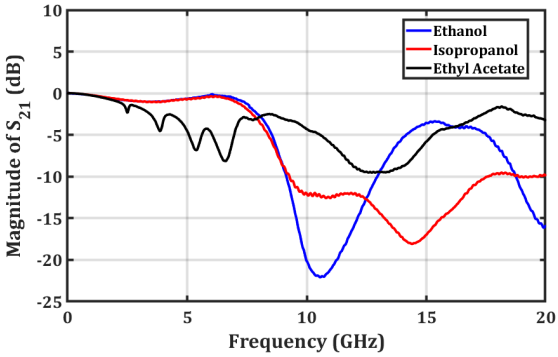

Fig. 24. Magnitude of de-embedded S_{21} versus frequency for copper sensors filled with ethanol, isopropanol, and ethyl acetate.

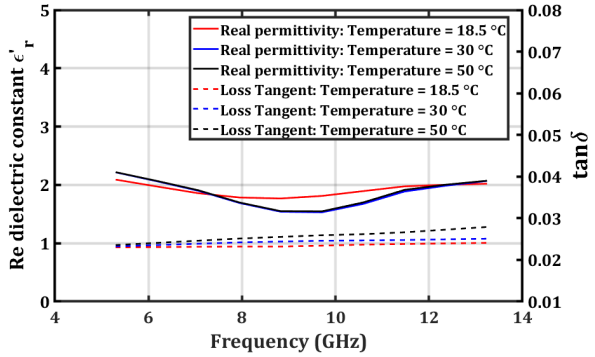

Fig. 23. Comparison of the real part of permittivity (left *y*-axis) and loss tangent (right *y*-axis) against frequency at different temperatures for $MgSO_4{\cdot}7H_2O$ filled in the small aluminum sensor.

escalates with temperature, with the trend being especially prominent at elevated temperatures and frequencies, indicating increased dielectric losses.

E. Liquids

Our experimental results, particularly with ethanol, isopropanol, and ethyl acetate, underscore the strong electromagnetic absorption properties of liquids. The S-parameters were measured by placing the liquids in small and medium-sized copper sensors. However, as shown in Fig. 24, the high dielectric constants and conductivity in these liquids led to significant wave absorption, effectively suppressing the resonant behavior. As a result, our method has limitations for measuring complex permittivity from S-parameters primarily due to the absence of resonance.

Further study is needed to accurately measure the complex permittivity of liquids using our method. One possible approach is to use a different type of sensor that is specifically designed for liquid materials. In addition, other measurement techniques, such as quality factor calculation, may need to be used to accurately measure the complex permittivity of liquids.

VI. Conclusion

A novel sensor was proposed for measuring the complex permittivity of solid, crystal grains, and powder dielectrics for a frequency range of 3–15 GHz. It comprises of an enclosure made of copper or aluminum, covered by a lid with an aperture, over which is an SL. Experiments conducted on seven different materials using four different sensors of different dimensions and materials demonstrated that the sensors can measure complex permittivity across a wide frequency range.

Our analyses highlighted that sensors, even with varied sizes, produce consistent readings. Minor discrepancies were observed in resonance frequencies and complex permittivity metrics, but these differences were minimal in most practical contexts. The complex permittivity was comparable above 6 (medium sensor) and 8 GHz (small sensor), with slightly larger deviations at lower frequencies.

Moreover, our examinations revealed a distinct inverse correlation between the enclosure's dimensions and the operative frequency range, with larger sensors exhibiting resonance near 4 GHz, thereby enabling reliable evaluations commencing from this frequency. An extensive study of temperature effects was also conducted, using $MgSO_4{\cdot}7H_2O$ as a representative dielectric. This disclosed interesting results, particularly with dielectric loss. It was observed that both the temperature and frequency play a pivotal role in increasing the rate of increase in dielectric loss, showcasing the intricate interdependencies between these variables.

In conclusion, this study highlights the strength and flexibility of our proposed method and sensor design and shows its effectiveness in measuring the complex permittivity of various materials. By systematically comparing our findings with those from prior studies, and experimenting with sensors of varying sizes and materials, we have provided a thorough and reliable method. This not only enhances our current understanding but also paves the way for further explorations into the nuanced properties of materials in electromagnetic realms and other closely aligned disciplines

Acknowledgment

The authors are grateful to Dr. Alireza Ghaneizadeh for his support and guidance throughout this project. They also thank Prof. Dr. Giuseppe Thadeu Freitas de Abreu and Prof. Dr. Werner Henkel for their support and provision of essential experimental equipment. Uwe Pagel's contribution to the sensor fabrication process is greatly appreciated. They are also grateful to Prof. Dr. Thomas Nugent and Thomas Schwarzlose for their assistance in providing the necessary chemicals.

Finally, they extend their profound thanks to Constructor University, Bremen, Germany, for the support throughout the research endeavor.

REFERENCES

[1] M. Joodaki and M. Rezaee, "Coplanar waveguide (CPW) loaded with an electromagnetic bandgap (EBG) structure: Modeling and application to displacement sensor," *IEEE Sensors J.*, vol. 16, no. 9, pp. 3034–3040, May 2016.

[2] J. Basseri and M. Joodaki, "Realization of a low-cost displacement sensor on PCB with two-metal-layer coplanar waveguide loaded by an EBG structure," *IEEE Sensors J.*, vol. 17, no. 15, pp. 4797–4804, Aug. 2017.

[3] J. Basseri and M. Joodaki, "An angular displacement sensor with a curved two-metal-layer CPW loaded by an EBG structure," *IEEE Sensors J.*, vol. 18, no. 6, pp. 2335–2341, Mar. 2018.

[4] S. E. Mohsir and M. Joodaki, "Design and implementation of SIW cavity oscillators for humidity sensing applications," in *Proc. 28th Iranian Conf. Electr. Eng. (ICEE)*, Tabriz, Iran, Aug. 2020, pp. 1–4.

[5] W. Wang et al., "Analysis and design of coil-based electromagnetic-induced thermoacoustic for rail internal-flaw inspection," *IEEE Trans. Intell. Transp. Syst.*, vol. 20, no. 7, pp. 2691–2702, Jul. 2019.

[6] W. Wang, Q. Cao, and Y. Zheng, "Bandstop frequency-selective structures based on stepped-impedance loop resonators: Design, analysis, and measurement," *IEEE Trans. Antennas Propag.*, vol. 67, no. 2, pp. 1053–1064, Feb. 2019.

[7] W. Wang, S. Yang, Z. Fang, Q. Sun, Y. Chen, and Y. Zheng, "Compact dual-polarized wideband antenna with dual-/single-band shifting for microbase station applications," *IEEE Trans. Antennas Propag.*, vol. 69, no. 11, pp. 7323–7332, Nov. 2021.

[8] W. Wang et al., "MRC-based double figure-of-eight coil sensor system with triple-mode operation capability for biomedical applications," *IEEE Sensors J.*, vol. 21, no. 13, pp. 14491–14502, Jul. 2021.

[9] W. Wang et al., "Novel coil transducer induced thermoacoustic detection of rail internal defects towards intelligent processing," *IEEE Trans. Ind. Electron.*, vol. 71, no. 2, pp. 2100–2111, Feb. 2024.

[10] J. Mu noz-Enano, P. Vélez, M. Gil, and F. Martín, "Planar microwave resonant sensors: A review and recent developments," *Appl. Sci.*, vol. 10, no. 7, p. 2615, Apr. 2020.

[11] P. Mehrotra, B. Chatterjee, and S. Sen, "EM-wave biosensors: A review of RF, microwave, mm-wave and optical sensing," *Sensors*, vol. 19, no. 5, p. 1013, Feb. 2019.

[12] P. Mezzanotte, V. Palazzi, F. Alimenti, and L. Roselli, "Innovative RFID sensors for Internet of Things applications," *IEEE J. Microw.*, vol. 1, no. 1, pp. 55–65, Jan. 2021.

[13] R. A. Alahnomi et al., "Review of recent microwave planar resonator-based sensors: Techniques of complex permittivity extraction, applications, open challenges and future research directions," *Sensors*, vol. 21, no. 7, p. 2267, Mar. 2021.

[14] J. Peng, S. Jia, J. Bian, S. Zhang, J. Liu, and X. Zhou, "Recent progress on electromagnetic field measurement based on optical sensors," *Sensors*, vol. 19, no. 13, p. 2860, Jun. 2019.

[15] U. C. Hasar, J. J. Barroso, M. Bute, Y. Kaya, M. E. Kocadagistan, and M. Ertugrul, "Attractive method for thickness-independent permittivity measurements of solid dielectric materials," *Sens. Actuators A, Phys.*, vol. 206, pp. 107–120, Feb. 2014.

[16] J. Leroy et al., "Microfluidic biosensors for microwave dielectric spectroscopy," *Sens. Actuators A, Phys.*, vol. 229, pp. 172–181, Jun. 2015.

[17] M. G. Douglas et al., "An algorithm for predicting the change in SAR in a human phantom due to deviations in its complex permittivity," *IEEE Trans. Electromagn. Compat.*, vol. 51, no. 2, pp. 217–226, May 2009.

[18] K. Staszek, A. Rydosz, E. Maciak, K. Wincza, and S. Gruszczynski, "Six-port microwave system for volatile organic compounds detection," *Sens. Actuators B, Chem.*, vol. 245, pp. 882–894, Jun. 2017.

[19] Z. Caijun, J. Quanxing, and J. Shenhui, "Calibration-independent and position-insensitive transmission/reflection method for permittivity measurement with one sample in coaxial line," *IEEE Trans. Electromagn. Compat.*, vol. 53, no. 3, pp. 684–689, Aug. 2011.

[20] N. M. Haase, G. Fuge, H. K. Trieu, A.-P. Zeng, and A. F. Jacob, "Miniaturized transmission-line sensor for broadband dielectric characterization of biological liquids and cell suspensions," *IEEE Trans. Microw. Theory Techn.*, vol. 63, no. 10, pp. 3026–3033, Oct. 2015.

[21] P. López-Rodríguez et al., "Comparison of metal-backed free-space and open-ended coaxial probe techniques for the dielectric characterization of aeronautical composites," *Sensors*, vol. 16, no. 7, p. 967, Jun. 2016.

[22] W. Liu, L. Xu, X. Yang, Y. Shi, and H. Zhan, "Complex permittivity determination based on a radio frequency device," *Sens. Actuators A, Phys.*, vol. 272, pp. 75–82, Apr. 2018.

[23] T. Reinecke, L. Hagemeier, H. Spehlbrink, S. Guenther, M. Klintschar, and S. Zimmermann, "Open-ended coaxial probe for the quantification of edema in human brain tissue," *Sens. Actuators B, Chem.*, vol. 204, pp. 763–769, Dec. 2014.

[24] M. Olyphant and J. H. Ball, "Strip-line methods for dielectric measurements at microwave frequencies," *IEEE Trans. Elect. Insul.*, vol. EI-5, no. 1, pp. 26–32, Mar. 1970.

[25] D. K. Ghodgaonkar, V. V. Varadan, and V. K. Varadan, "A free-space method for measurement of dielectric constants and loss tangents at microwave frequencies," *IEEE Trans. Instrum. Meas.*, vol. 38, no. 3, pp. 789–793, Jun. 1989.

[26] D. Li, C. E. Free, K. E. G. Pitt, and P. G. Barnwell, "A simple method for accurate loss tangent measurement of dielectrics using a microwave resonant cavity," *IEEE Microw. Wireless Compon. Lett.*, vol. 11, no. 3, pp. 118–120, Mar. 2001.

[27] P. Sharma, L. Lao, and G. Falcone, "A microwave cavity resonator sensor for water-in-oil measurements," *Sens. Actuators B, Chem.*, vol. 262, pp. 200–210, Jun. 2018.

[28] A. Raveendran and S. Raman, "Complex permittivity extraction of planar dielectrics using a noninvasive microwave transmission line resonant technique," *IEEE Trans. Instrum. Meas.*, vol. 70, 2021, Art. no. 6006708.

[29] *Measurement of Dielectric Material Properties*, Rhode & Schwarz, Munich, Germany, 2012.

[30] J. Krupka, "Frequency domain complex permittivity measurements at microwave frequencies," *Meas. Sci. Technol.*, vol. 17, no. 6, pp. R55–R70, Apr. 2006.

[31] J. M. Catala-Civera, A. J. Canos, F. L. Penaranda-Foix, and E. de los Reyes Davo, "Accurate determination of the complex permittivity of materials with transmission reflection measurements in partially filled rectangular waveguides," *IEEE Trans. Microw. Theory Techn.*, vol. 51, no. 1, pp. 16–24, Jan. 2003.

[32] M. D. Janezic, D. F. Williams, V. Blaschke, A. Karamcheti, and C. S. Chang, "Permittivity characterization of low-k thin films from transmission-line measurements," *IEEE Trans. Microw. Theory Techn.*, vol. 51, no. 1, pp. 132–136, Jan. 2003.

[33] H. Shwaykani, A. El-Hajj, J. Costantine, and M. Al-Husseini, "A calibration-free method for the dielectric constant calculation of low-loss materials," *IEEE Trans. Instrum. Meas.*, vol. 70, 2021, Art. no. 6000310.

[34] C. K. Campbell, "Free-space permittivity measurements on dielectric materials at millimeter wavelengths," *IEEE Trans. Instrum. Meas.*, vol. IM-27, no. 1, pp. 54–58, Mar. 1978.

[35] Y. Wang, X. Shang, N. M. Ridler, T. Huang, and W. Wu, "Characterization of dielectric materials at WR-15 band (50–75 GHz) using VNA-based technique," *IEEE Trans. Instrum. Meas.*, vol. 69, no. 7, pp. 4930–4939, Jul. 2020.

[36] U. C. Hasar et al., "Improved method for permittivity determination of dielectric samples by free-space measurements," *IEEE Trans. Instrum. Meas.*, vol. 71, 2022, Art. no. 6002108.

[37] D. Popovic et al., "Precision open-ended coaxial probes for in vivo and ex vivo dielectric spectroscopy of biological tissues at microwave frequencies," *IEEE Trans. Microw. Theory Techn.*, vol. 53, no. 5, pp. 1713–1722, May 2005.

[38] F. E. Gardiol, *Open-Ended Waveguides: Principles and Applications*. Amsterdam, The Netherlands: Elsevier, 1985, pp. 139–187.

[39] M. Hirano, M. Takahashi, and M. Abe, "A measurement of complex permittivity of lossy dielectrics by using flanged rectangular waveguide," *Electron. Commun. Jpn. (II: Electron.)*, vol. 84, no. 4, pp. 59–67, Mar. 2001.

[40] Y. Wang and M. N. Afsar, "Measurement of complex permittivity of liquids using waveguide techniques," *Prog. Electromagn. Res.*, vol. 42, pp. 131–142, 2003.

[41] N. Kazemi, M. Abdolrazzaghi, P. E. Light, and P. Musilek, "In–human testing of a non-invasive continuous low–energy microwave glucose sensor with advanced machine learning capabilities," *Biosensors Bioelectron.*, vol. 241, Dec. 2023, Art. no. 115668.

[42] M. Abdolrazzaghi, N. Kazemi, V. Nayyeri, and F. Martin, "AI-assisted ultra-high-sensitivity/resolution active-coupled CSRR-based sensor with embedded selectivity," *Sensors*, vol. 23, no. 13, p. 6236, Jul. 2023.

[43] L. Su, J. Mata-Contreras, P. Velez, and F. Martin, "Splitter/combiner microstrip sections loaded with pairs of complementary split ring resonators (CSRRs): Modeling and optimization for differential sensing applications," *IEEE Trans. Microw. Theory Techn.*, vol. 64, no. 12, pp. 4362–4370, Dec. 2016.

[44] B. Salski, J. Cuper, T. Karpisz, P. Kopyt, and J. Krupka, "Complex permittivity of common dielectrics in 20–110 GHz frequency range measured with a Fabry–Pérot open resonator," *Appl. Phys. Lett.*, vol. 119, no. 5, Aug. 2021, Art. no. 052902.

[45] B. Salski, P. Czekala, T. Karpisz, and P. Kopyt, "Mode coupling in a Fabry–Pérot open resonator," *IEEE Trans. Microw. Theory Techn.*, vol. 70, no. 1, pp. 299–306, Jan. 2022.

[46] H. Chen, H. Chen, W. Che, S. Zheng, X. Xiu, and Q. Xue, "Review and modification of permittivity measurement on open resonator for transparent material measurements at terahertz," *IEEE Trans. Instrum. Meas.*, vol. 69, no. 11, pp. 9144–9156, Nov. 2020.

[47] X. Bao et al., "Coplanar waveguide for dielectric material measurements at frequencies from 140 GHz to 220 GHz," in *Proc. 90th ARFTG Microw. Meas. Symp. (ARFTG)*, Nov. 2017, pp. 1–4.

[48] T. Chretiennot, D. Dubuc, and K. Grenier, "A microwave and microfluidic planar resonator for efficient and accurate complex permittivity characterization of aqueous solutions," *IEEE Trans. Microw. Theory Techn.*, vol. 61, no. 2, pp. 972–978, Feb. 2013.

[49] W. L. Nicholson and G. F. Ross, "Theory and application of the four-parameter transmission-line network," *Bell Syst. Tech. J.*, vol. 49, no. 1, pp. 107–126, 1970.

[50] A. N. Vicente, G. M. Dip, and C. Junqueira, "The step by step development of NRW method," in *IEEE MTT-S Int. Microw. Symp. Dig.*, Oct. 2011, pp. 738–742.

[51] J. Baker-Jarvis, E. J. Vanzura, and W. A. Kissick, "Improved technique for determining complex permittivity with the transmission/reflection method," *IEEE Trans. Microw. Theory Techn.*, vol. 38, no. 8, pp. 1096–1103, Aug. 1990.

[52] J. Baker-Jarvis et al., "Measuring the permittivity and permeability of lossy materials: Solids, liquids, metals, and negative-index materials," Nat. Inst. Standards Technol. (NIST), Gaithersburg, MD, USA, Tech. Rep. 1536, Feb. 2005.

[53] A. Shourvarzi and M. Joodaki, "Shielding effectiveness estimation of an enclosure with an arbitrary shape aperture," in *Proc. Int. Symp. Electromagn. Compat. (EMC Eur.)*, Sep. 2017, pp. 1–4.

[54] A. Shourvarzi and M. Joodaki, "Shielding effectiveness estimation of a metallic enclosure with an aperture using S-parameter analysis: Analytic validation and experiment," *IEEE Trans. Electromagn. Compat.*, vol. 59, no. 2, pp. 537–540, Apr. 2017.

[55] A. Shourvarzi and M. Joodaki, "Using aperture impedance for shielding effectiveness estimation of a metallic enclosure with multiple apertures on different walls considering higher order modes," *IEEE Trans. Electromagn. Compat.*, vol. 60, no. 3, pp. 629–637, Jun. 2018.

[56] A. Shourvarzi and M. Joodaki, "Shielding effectiveness measurement for extremely small dimension enclosures," *IEEE Trans. Electromagn. Compat.*, vol. 61, no. 6, pp. 1740–1745, Dec. 2019.

[57] I. Dilman, M. N. Akinci, T. Yilmaz, M. Çayören, and I. Akduman, "A method to measure complex dielectric permittivity with open-ended coaxial probes," *IEEE Trans. Instrum. Meas.*, vol. 71, 2022, Art. no. 6000507.

[58] R. Mavaddat, *Network Scattering Parameters*. Singapore: World Scientific, Mar. 1996.

[59] D. K. Cheng, *Field and Wave Electromagnetics*, 2nd ed. Boston, MA, USA: Addison-Wesley, 1989.

[60] D. Di Marco et al., "Dielectric properties of pure alumina from 8 GHz to 73 GHz," *J. Eur. Ceram. Soc.*, vol. 36, no. 14, pp. 3355–3361, Nov. 2016.

[61] C. Liu et al., "Dielectric properties and microwave heating characteristics of sodium chloride at 2.45 GHz," *High Temp. Mater. Processes*, vol. 32, no. 6, pp. 587–596, Dec. 2013.

[62] M. Hotta, M. Hayashi, A. Nishikata, and K. Nagata, "Complex permittivity and permeability of SiO_2 and Fe_3O_4 powders in microwave frequency range between 0.2 and 13.5 GHz," *ISIJ Int.*, vol. 49, no. 9, pp. 1443–1448, 2009.

[63] R. D. Geryak, J. W. Schultz, Z. Borders, J. G. Maloney, J. G. Calzada, and J. T. Welter, "New method for determining permittivity of thin polymer sheets," in *Proc. Antenna Meas. Techn. Assoc. Symp. (AMTA)*, Oct. 2021, pp. 1–6.

[64] M. D. Deshpande, C. J. Reddy, P. I. Tiemsin, and R. Cravey, "A new approach to estimate complex permittivity of dielectric materials at microwave frequencies using waveguide measurements," *IEEE Trans. Microw. Theory Techn.*, vol. 45, no. 3, pp. 359–366, Mar. 1997.

[65] R. L. Cravey et al., "Dielectric property measurements in the electromagnetic properties measurement laboratory," NASA, Washington, DC, USA, Tech. Rep. 110147, Apr. 1995.

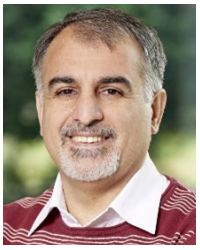

Mojtaba Joodaki (Senior Member, IEEE) received the B.Sc. degree in electrical and electronic engineering from Iran Science and Technology University, Tehran, Iran, in 1994, the M.Sc. degree in electrical and electronic engineering from Tarbiat Modarres University, Tehran, in 1997, and the Ph.D. degree in electrical engineering from Kassel University, Kassel, Germany, in 2002.

He joined ATMEL Germany GmbH, Heilbronn, Germany, as a Device Engineer, in 2002, where he was working on technology development, modeling, and characterization of Si- and SiGe-based devices for RF applications. In April 2005, he joined Infineon Technologies AG, Munich, Germany, as a Development Engineer, where he was responsible for electromagnetic interference (EMI)/electromagnetic compatibility (EMC) of memory modules. In his last industrial position, from October 2006 to July 2009, he was a Device Engineer with Qimonda GmbH, Dresden, Germany, involved in developing nanotransistors for dynamic random access memory (DRAM) products. Then, he started working as a Visiting Scientist and a Lecturer with the Institute of Nanostructure Technologies and Analytics (INA), Kassel University, where he defended his Habilitation dissertation in April 2011. In 2010, he joined the Department of Electrical Engineering, Ferdowsi University of Mashhad, Mashhad, Iran, as an Assistant Professor of Electronic Engineering (RF Circuit Design and Semiconductor Devices and Technology), where he was promoted to an Associate Professor in September 2011 and a Professor in July 2018. Since January 2020, he has been with Constructor University (former Jacobs University), Bremen, Germany, as a Professor of Electrical Engineering and Electrical, and the Computer Engineering Program Chair. His research interests include modeling, characterization, and fabrication of passive and active devices (organic and inorganic) for high-frequency, memory, and optoelectronic applications as well as EMC of electronic products.

Mr. Joodaki is a Life Member of the International Society for Optics and Photonics (SPIE). He has been awarded several prizes for his scientific activities, including the Best Dissertation Prize of North Hessen Universities from the Association of German Engineers (VDI) in 2004, the Young Graduated Research Fellowship of the Gallium Arsenide (GaAs) Association in the European Microwave Week 2001 and 2002, and the F-Made Scholarship of SPIE in 2002.

Roshan Nepal (Graduate Student Member, IEEE) was born in Urlabari, Morang, Nepal, in 2001. He received the B.Sc. degree in electrical and computer engineering (ECE) from Constructor University, Bremen, Germany, in 2023. He is currently pursuing the M.Sc. degree in ECE with the University of Waterloo, Waterloo, ON, Canada.

His research interests include electromagnetic compatibility (EMC), microwaves, and antennas.

Ali Shourvarzi, photograph and biography not available at the time of publication.